Brief communication: Impact of swell waves on atmospheric surface turbulence: A wave-turbulence decomposition method

Mostafa Bakhoday Paskyabi[1]

[1]Geophysical Institute, Universtiy of Bergen, Bergen, Norway, and Bergen Offshore Wind Centre, Bergen, Norway
Correspondence: Mostafa Bakhoday Paskyabi (Mostafa.Bakhoday-Paskyabi@uib.no)

Abstract. To characterize the turbulence quantities such as vertical momentum fluxes during swell wave conditions, we develop a wave-turbulence decomposition method to split the high-frequency surface wind data into wind and wave time series. By assuming the frozen turbulence field, the method replaces an empirically fitted spectrum to the observed wind spectrum within the wave-affected frequency band. Time series of waves and turbulence are then synthetically generated based on a

5   proposed wind-wave coherence function. Using two days of sonic anemometer wind measurements at 15 m height, the upward momentum transfer could be observed during high-steady ($\sim$ 7 m/s) and decaying wind conditions. The vertical wind spectra show, however, higher energy within the wave frequency bands during low winds, old sea, and stable boundary layer condition. During the high and decaying winds, the atmospheric stability changes between unstable and stable conditions, blurring the wave signals due to the thermally/mechanically generated turbulence.

10 # 1   Introduction

Over the last several decades, a large number of laboratory studies and field experiments have shown modulation of turbulent momentum fluxes across a layer, so-called Wave Boundary Layer (WBL), on both sides of air-sea interface (Chalikov, 1995; Rieder et al., 1994). The height of this sublayer, for example in the atmosphere, is approximately few metres and in the order of significant wave height. The atmospheric WBL is then limited from bellow by the air-sea interface and at the top

15 by the atmospheric surface layer (in which the Monin–Obukhov Similarity Theory, MOST, is applied). Stratification may have direct and indirect impacts on the wind–wave interaction within the WBL (Semedo et al., 2009). However, such effects depend on the height of the WBL with respect to the height of the dynamic sublayer, wave age, and the relative angle between wind and wave directions. Within the WBL, particularly under the influence of swell waves (low to moderate wind speeds), the MOST or the logarithmic law cannot be applied in order to estimate the drag coefficient or roughness length, and the

20 wind profiles show a jet at top of the WBL (Chalikov and Rainchik, 2011). This is because waves excite perturbations in this sublayer in addition to contributions from the buoyancy and shear productions. Although studies over the last few decades have significantly improved understanding of turbulent flows above the surface gravity waves, detailed knowledge of WBL and its interaction with atmospheric turbulence under varying forcing conditions are key in better understanding of turbulent processes and enhancing the accuracy of turbulent closure schemes used in oceanic, atmospheric, climate, and offshore structural analysis

25 models (Bakhoday-Paskyabi et al., 2022).

In this study, we utilize a set of near-surface wind and wave measurements collected during OBLEX-F1 campaign from the FINO1 offshore meteorological mast in June 2015. Based on these data, we explore the turbulent structures above and within the WBL, and the interactions of waves and wind stress over different atmospheric stability and sea-state conditions. We further calculate the swell-induced momentum fluxes from both available theories and high frequency observational data.

30   This paper is organized as follows. In section 2, we will briefly explain the wave-turbulence decomposition and the estimation of wave-induced momentum fluxes. Section 3 explains measurements of wind and wave at FINO1 offshore met-mast, and Section 4 describes the verification results of suggested method. Section 5 provides a brief discussion and summary of the work.

2   Methods

35   In the presence of swell waves, we decompose the total wind $\boldsymbol{u} = (u, v, w)$ into the mean $\bar{\boldsymbol{u}}$, the turbulent $\boldsymbol{u}'$, and the wave $\tilde{\boldsymbol{u}}$ as

$$\boldsymbol{u} = \bar{\boldsymbol{u}} + \boldsymbol{u}' + \tilde{\boldsymbol{u}}, \tag{1}$$

where u, v, and w are horizontal and vertical velocity components respectively. Based on this decomposition, we will study in this section the wave boundary layer through the wave-turbulence decomposition.

40   ### 2.1   Wind-wave decomposition

To decompose wind and wave signals (or wave-turbulence decomposition), the energy spectrum of each velocity component in the inertial range at wavenumbers fairly above and below the wave band can be fitted using following 1D Kaimal wavenumber spectrum:

$$\frac{k F_{\beta\beta}(k)}{\sigma_\beta^2} = \frac{A(k/k_{0\beta})}{1 + (k/k_{0\beta})^{5/3}}, \tag{2}$$

45   where k denotes wavenumber, $\beta = u, v, w$, $A = 5\sin(3\pi/5)/(6\pi)$ is a constant, and $k_{0\beta}$ and σ_β are two adjustable parameters describing the roll-off wavenumber (the length scales of turbulent eddies in the energy-containing subrange) and the standard deviation of β, respectively (Gerbi et al., 2009). Wavenumber spectrum is converted to frequency scales by invoking Taylor's frozen turbulence hypothesis, $k = \omega/\bar{u}$ where $\omega = 2\pi f$ and $\bar{u}$ is the mean (advection) wind speed:

$$df E_{\beta\beta}(f) = dk F_{\beta\beta}(k). \tag{3}$$

50   Here $E_{\beta\beta}(f)$ is the frequency spectrum of the wind β-component, and the derivative dk/df is estimated by the use of the wave dispersion relation. We apply a two-parameter least squares fitting of the model spectrum in Eq. (2) to the measured spectrum. For fitting (in log–log space), we first determine the wave-affected band as $[0.6k_p, k_p + 0.1]$ (or $[0.6f_p, f_p + 0.1]$) at which k_p

(f_p) denotes the peak wavenumber (frequency) measured from the recorded wave peak period, T_p. The energy spectrum is then divided into three bands: below-wave-band ($k < 0.6k_p$), wave-band, and above-wave-band ($k > k_p + 0.1$) parts, see Fig.

55 1a and b. After discarding the wave-band, we fit the Kaimal spectrum Eq. (2) over below and above wave-band wavenumbers and replace the wave-induced bump by the fitted curve. The wave induced spectrum is then estimated as follows

$$E_{\tilde{\beta}\tilde{\beta}}(k) = E_{\beta\beta}(k) - E_{\beta'\beta'}(k). \tag{4}$$

To estimate time series of wave components in Eq. (4), we set $\boldsymbol{u} \leftarrow \boldsymbol{u} - \bar{\boldsymbol{u}}$ and transform Eq. (1) into the Fourier space in terms of Fourier coefficients of wind U_j, V_j, W_j and waves $\tilde{U}_j, \tilde{V}_j, \tilde{W}_j$, for example $E_{uu} = |U_j|$ and $E_{\tilde{u}\tilde{u}} = |\tilde{U}_j|$. These Fourier

60 coefficients are expressed in phasor notation as follows Bricker and Monismith (2007):

$$U_j = |U_j|e^{i\angle U_j}, \tag{5}$$
$$\tilde{U}_j = |\tilde{U}_j|e^{i\angle \tilde{U}_j}, \tag{6}$$

where $\angle$ denotes the phase operator, $i = \sqrt{-1}$ is the imaginary unit, and $|\cdot|$ represents the magnitude operator. By taking inverse Fourier transformation of above two-sided equations, we calculate the time series of turbulent and wave velocities (see

65 Eqs. 9 and 10).

2.2 Synthetic turbulence

To isolate the wave contributions from the wind fluctuation signal, we use the Davenport representation of coherence (Davenport, 1961) and suggest a wave coherence contribution as follows:

$$\gamma(z,f) = A_1 \exp\left(-C_1 \frac{fz}{\bar{u}}\right) + A_2 \cos\left[\frac{2\pi fz}{\beta_1 H_s/Tp} + \alpha\phi\right] \exp\left(-C_2\lambda_w \frac{(f-f_p)^2 z}{\beta_2(H_s/T_p)^2}\right), \tag{7}$$

70 where C_1, C_2, A_1, A_2, β_1 and β_2 are empirically determined coefficients. Oscillations of wave component are controlled by setting a small value for the random phase-shift of ϕ (i.e. $\alpha \sim 0.1$). Here, f is frequency, z is height from the surface, $\bar{u}$ denotes the mean wind speed, and λ_w is the wave length determined by utilising the dispersion relation and values of wave peak period, T_p, and the significant wave height, H_s. By estimating the squared coherence, γ^2, between vertical wind w and wave elevation η in the frequency domain, the spectral density of the wave induced and turbulence fluctuations at the height of z are given

75 according to Eq. (4) Rieder et al. (1994):

$$E_{w'w'}(f) = (1-\gamma^2)E_{ww}, \quad \text{and} \quad E_{\tilde{w}\tilde{w}}(f) = \gamma^2 E_{ww}. \tag{8}$$

The random realizations of the wind and wave time series for vertical velocity are then estimated according to

$$w'(t) = \Sigma_i \sqrt{2E_{w'w'}(f)\Delta f}[r_i^{(1)}\cos(\omega t) + r_i^{(2)}\sin(\omega t)], \tag{9}$$
$$\tilde{w}(t) = \Sigma_i \sqrt{2E_{\tilde{w}\tilde{w}}(f)\Delta f}[q_i^{(1)}\cos(\omega t) + q_i^{(2)}\sin(\omega t)], \tag{10}$$

80 where $r_i^{(1)}, r_i^{(2)}, q_i^{(1)}$ and $q_i^{(2)}$ are normal random numbers. In the synthetic time series, we determine the bulk wave parameters using $H_s = 0.0248|U_{10}|^2$ and $T_p = 0.729|U_{10}|$ (Carter, 1982), where U_{10} indicates the wind speed at 10 m height.

WIND
ENERGY
SCIENCE
DISCUSSIONS

eawe
european academy of wind energy

2.3 Air-sea momentum flux

According to Eq. (1), the momentum flux at the surface, to the leading order, can be written as

$$\boldsymbol{\tau}(z) = \boldsymbol{\tau}_\nu + \boldsymbol{\tau}_f(z), \tag{11}$$

where $\boldsymbol{\tau}_\nu$ and $\boldsymbol{\tau}_f(z)$ are the viscous stress and form stress at the height of z respectively (Donelan et al., 2012). By assuming that waves decay exponentially in vertical, the wave form stress at z is defined by

$$\boldsymbol{\tau}_f(z) = \rho_w \int\limits_{k_{min}}^{k_{max}} \int\limits_{-\pi}^{\pi} e^{-2kz} \beta_g(k,\theta) \omega F(k,\theta) \boldsymbol{k} d\theta dk, \tag{12}$$

where $F(k,\theta)$ is the 2D wave variance spectrum, θ denotes the wave direction, ρ_w is the water density, and k_{min} and k_{max} are the minimum and maximum of wavenumbers. β_g is the wave growth rate as a function of wind speed at the height of $\lambda/2$ (i.e. $u_{\lambda/2}$ calculated by the logarithmic wind profile, where λ is the wavelength):

$$\beta_g(k,\theta) = A\omega \frac{\rho_a}{\rho_w} \frac{[u_{\lambda/2}\cos(\theta-\theta_w)]|u_{\lambda/2}\cos(\theta-\theta_w)|}{c^2}, \tag{13}$$

where θ_w indicates the wind direction, c is the wave phase speed, and the proportionality coefficient A is expressed by (Donelan et al., 2012):

$$A = \begin{cases} 0.11 & u_{\lambda/2}\cos(\theta) > c & \text{(wind sea)} \\ 0.01 & 0 < u_{\lambda/2}\cos(\theta) < c & \text{(fast running swell)}. \\ 0.1 & \cos(\theta) < 0 & \text{(swellopposing the wind)} \end{cases}$$

The form drag is calculated using the friction velocity and the wind speed at a reference height of z (i.e. u_z) as $Cd_f = (u_*/u_z)^2$. The viscous stress is expressed by

$$\boldsymbol{\tau}_\nu = \rho_a Cd'_\nu |u_z| u_z, \tag{14}$$

where the adjusted viscous drag by the form drag (sheltering effect) is given by

$$Cd'_\nu = \frac{Cd_\nu}{3}\left(1 + \frac{2Cd_\nu}{Cd_\nu + Cd_f}\right) \tag{15}$$

where Cd_ν is the viscous drag coefficient.

3 Data

3.1 Dataset

The FINO1 measurement mast in the North Sea is located about 45 km north of the Borkum island, Germany. Its geographical coordinates are $54^o0'53.5''$ N, and $6^o35'15.5''$ E. The water depth at FINO1 is approximately 30 m and the mast height is 100

105 m above the mean sea level. The site is exposed to an unlimited fetch area for northwesterly and northerly winds (Bakhoday-Paskyabi et al., 2018). The mast is equipped with different meteorological sensors such as cup anemometers to measure the velocity at 33, 40, 50, 60, 70, 80, 90 and 100 m, and sonic anemometers with a sampling frequency of 10 Hz at 40, 60 and 80 m (Fig. 2b). During the OBLEX-F1 campaign between 2015 and 2016 two additional sonic anemometers were installed at 15 and 20 m above the mean sea level with sampling frequency of 25 Hz. We use only the data from the one installed at 15

110 m height in this study. Furthermore, we use wave frequency spectra recorded by an AXYS wave buoy in the close vicinity of FINO1 platform during the study period.

3.2 Data Analysis

Figure 1 shows time series of wind, wave, and stability parameter during the study period in June 2015. We do not exclude the effect of flow distortions by the FINO1 mast when the spectra show very clear wave-induced elevation (for wind directions

115 between 245° and 360°). Wind speed, U_{10}, ranges from moderate to high wind ($2 \leq U_{10} < 11$ ms^{-1}, Fig. 1a), and during the strong wind-wave interactions (after June 24), the wind and wave directions are mostly misaligned (with direction differences larger than 100°). We study two cases representing the opposed-wind and swell conditions (vertical dashed lines). Figure 1c shows the atmospheric stability parameter z/L at a height of $z = 15$ m where

$$L = -\frac{u_*^3 \bar{\theta}_v}{g\kappa(\overline{w'\theta'_v})},$$

120 denotes the Obukhov length scale, κ and g are the von Kármán constant and the gravitational acceleration. $\overline{w'\theta'_v}$ is the flux of virtual potential temperature, and $\bar{\theta}_v$ denotes the virtual potential temperature. The stability changes from stable ($L > 0$) to unstable ($L < 0$), and both study episodes represent, on average, stable conditions ($L = 300$ and 203 m respectively).

4 Results

The theoretical (normalised) coherence spectra for two different wind speeds are obtained by Eq. (7). Figure 2a shows that

125 the coherence functions have peak values at f_p with an exponential decay beyond the wave band, where f_p is the wave peak frequency in Hz. The decay coefficients for both wind and wave components in Eq. (7) are set to constant values for the sake of simplicity ($C_1 = C_2 = 1$) and do not increase by increasing the wind speed. From the procedure given in Section 2.2 and coherence information drawn in Fig. 2a, we obtain realisations of turbulent winds for two cases, with wind speeds of $U_{10} = 10$ and 20 m/s respectively. The spectral energy distributions of synthetically generated winds are shown in Fig. 2b

130 that identifies the impact of waves on the turbulence in the inertial subrange, particularly across the wave frequency band, $0.7f_p \leq f \leq f_p + 0.1$. Figures 2c and d show the fitting of the model spectrum from Eq. (2) for the vertical wind in order to the synthetically generate the spectra of turbulent fluctuations within the wave frequency band (i.e. blue curves, see Section 2.1).

Figure 3a shows the time variation of the wave age, χ, during the study period covering both the mixed wind-sea (i.e. $\chi < 1.2$) and the swell waves (i.e. $\chi \geq 1.2$). Wind and waves are obviously aligned during the wind-sea conditions. For the conditions

135 where the swell waves are dominant (see Fig. 3b), wind and waves are mainly misaligned with a difference approximately more
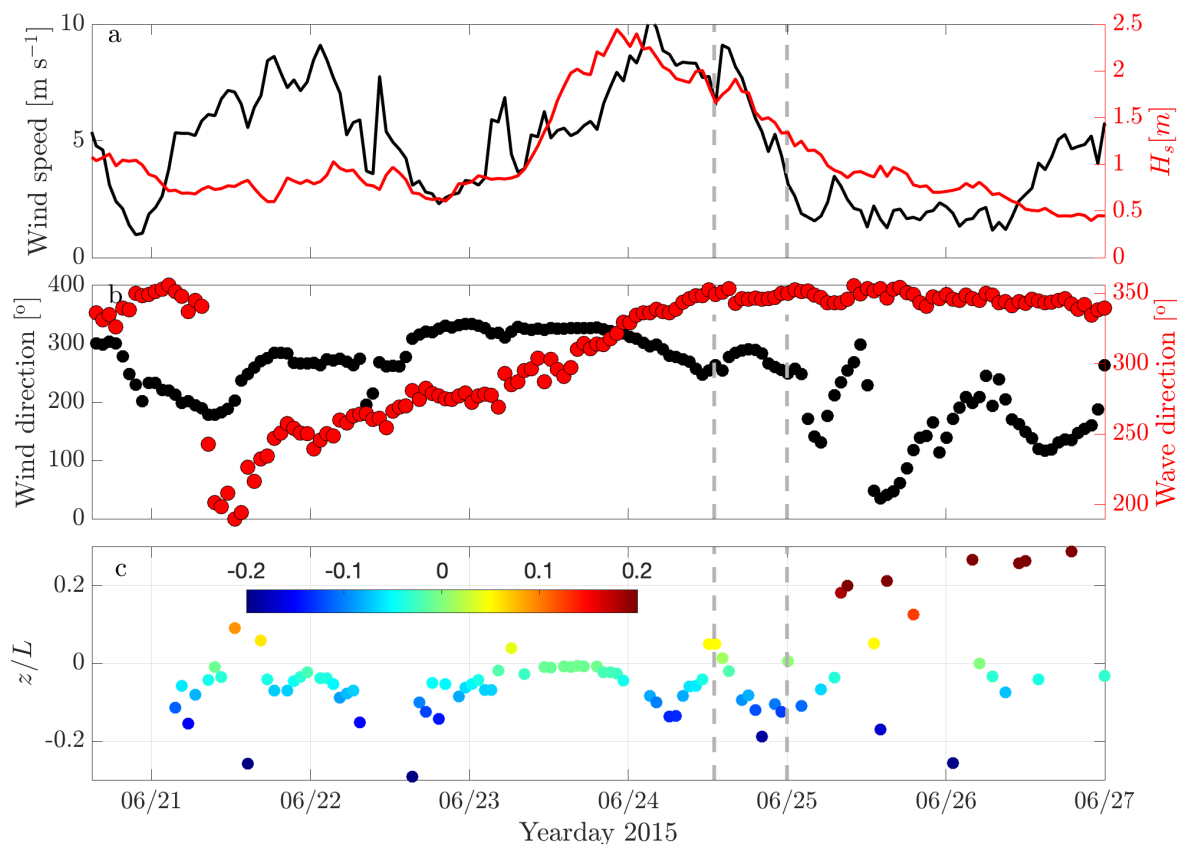
Figure 1. (a) Times series of wind speed at 10 m height measured by the FINO1's cup anemometer (black line) and significant wave height (red line) measured by a floating buoy operating in the close vicinity of FINO1 platform; (b) wind (black markers) and wave (red markers); and (c) values of the Obukhov length, L, calculated from sonic measurement at height of 15 m above the mean sea level collected with sampling frequency of 25 Hz between 21 and 27 June 2015. The stability classes have been color-coded in this figure. Vertical grey dashed lines highlight the study events of wind-wave interaction at 24th June at 13:00 and 25th June at 00:00, respectively.
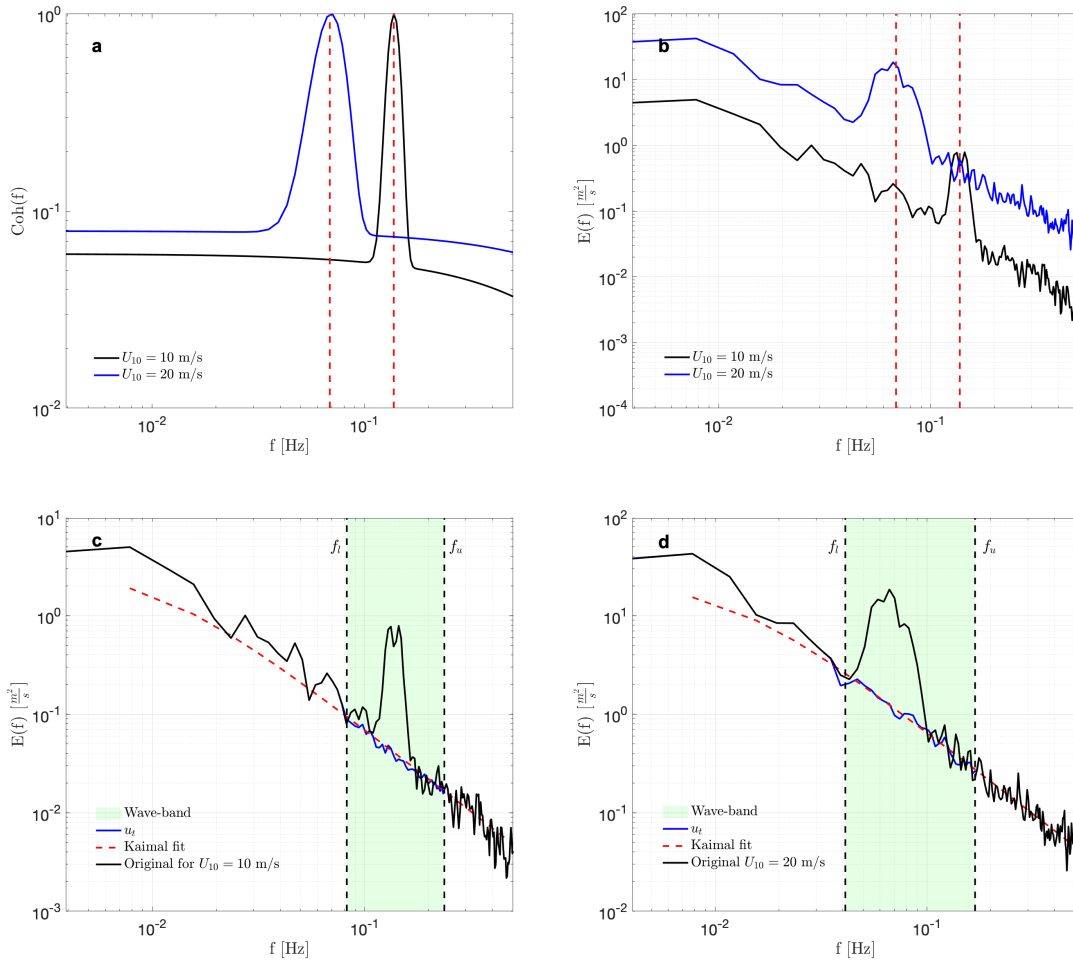
Figure 2. (a) Coherence functions of the wind and wave for $A_1/A_2 = 7.5$ in Eq. (7) (before normalising the total coherence) with peak wave frequencies of $f_p = 0.14$ Hz and $f_p = 0.06$ Hz corresponding to wind speeds of 10 and 20 m/s respectively; (b) the energy spectra of the vertical velocity w estimated from the Kaimal spectra Eq. (2) for two study cases; (c) the energy spectrum of the first case with $U_{10} = 10$ m/s and $f_p = 0.14$ Hz (black line) and the corrected spectrum (blue line); and (d) the energy spectrum of the first case with $U_{10} = 20$ m/s and $f_p = 0.06$ Hz (black line) and the corrected spectrum (blue line). The red dashed lines drawn in (c) and (d) show the spectral curves calculated from Eq. (2). Furthermore, the green-coloured areas in these figures represent the wave-affected frequency band with lower and upper frequencies of $f_l = 0.7 f_p$ and $f_u = f_p + 0.1$, respectively.

than 100°. This is particularly the case after 25 June when the wind-wave misalignment shows an oscillation-like behaviour. The atmosphere experiences mainly stable and also in lesser extent unstable conditions during this period (see Fig. 1c). The time-evolution of the power spectral density of the vertical wind speed (i.e. w-component) is presented in Fig. 3c. This figure has been overlaid by the time series of the wave peak frequency, f_p. There is a good agreement between the measured f_p

140 and the spectral peak of the measure vertical component wind at the wave frequency band, consistent with an increase in the values of wave age (i.e. values of χ greater than 1.2). While the agreement is better if the atmosphere is stable, but it is weakly pronounced in the presence of unstable conditions particularly after June 25.

To investigate the ability of the suggested method in splitting the fluctuations of wave and turbulence, we use 30-min time series of sonic anemometer data at 15 m height for two study events (Fig. 4). These events correspond to strong swell-wind

145 interaction, characterised by low wind, large values of χ, and spectrally enhanced energy within the wave-affected frequency band (i.e. around f_p). The spectra of the corrected vertical velocity fluctuations w' and the vertical wave $\tilde{w}$ are then shown in Fig. 4c and d. It is observed how the decomposition detaches the wave-induced energy elevation from the inertial subrange of w.

Regarding to the calculation of momentum flux, splitting between wave and wind fluctuations is not reasonable if there is no

150 obvious footprint of waves in the measured velocity spectra at 15 m height. As a result, the decomposition algorithm is applied if the ratio of the energy variances in the wave frequencies and model spectrum, R, is larger than 1:

$$R = \frac{\int_{f_l}^{f_u} E_{ww}^o(f)df}{\int_{f_l}^{f_u} E_{ww}^m(f)df} > 1, \tag{16}$$

where E_{ww}^o and E_{ww}^m are the sonic based energy spectrum and the model spectrum of the vertical wind speed given by Eq. (2), respectively. Figure 5a shows a measure to assess the strength of wavy structures in the observed velocity spectra. We

155 apply the decomposed turbulence time series when $R > 1$ (i.e. there exists a well-pronounced energy elevation around f_p). The estimated values of τ using Eq. (11) is almost consistent with COARE3 results (Edson et al., 2013) when $R < 1$. The wave momentum decreases from positive to negative for the swells propagating opposed to the wind direction (i.e. $R > 1$, see Fig. 5b and Fig. 3a). Figure 5c shows that the estimated $\tilde{\tau}$ at $z = 15$ m using Eq. (11) is approximately in acceptable agreement with the measured $\tilde{\tau}$ from the sonic data. In estimated $\tilde{\tau}$, the dimensionless function for the vertical decay plays a significant

160 role that its importance will be explored elsewhere.

5 Conclusions

We have suggested a wind-wave decomposition algorithm for the turbulent airflow over the ocean in the presence of swell waves based on high frequency data recorded from a sonic anemometer at 15 m height above the mean sea level. We have also proposed an empirical formulation for the coherence to account for both fluctuating wind and the effects of swell waves.

165 While the model has been used to generate idealised time series of wind under swell conditions, it can be also fitted with observational data. Furthermore, we quantified the wave-induced stresses by assuming both a certain growth rate and vertical decay function. Two real cases during the opposed wind-wave conditions were selected to demonstrate physical aspects of wind

WIND
ENERGY
SCIENCE
DISCUSSIONS

eawe
european academy of wind energy

Open Access
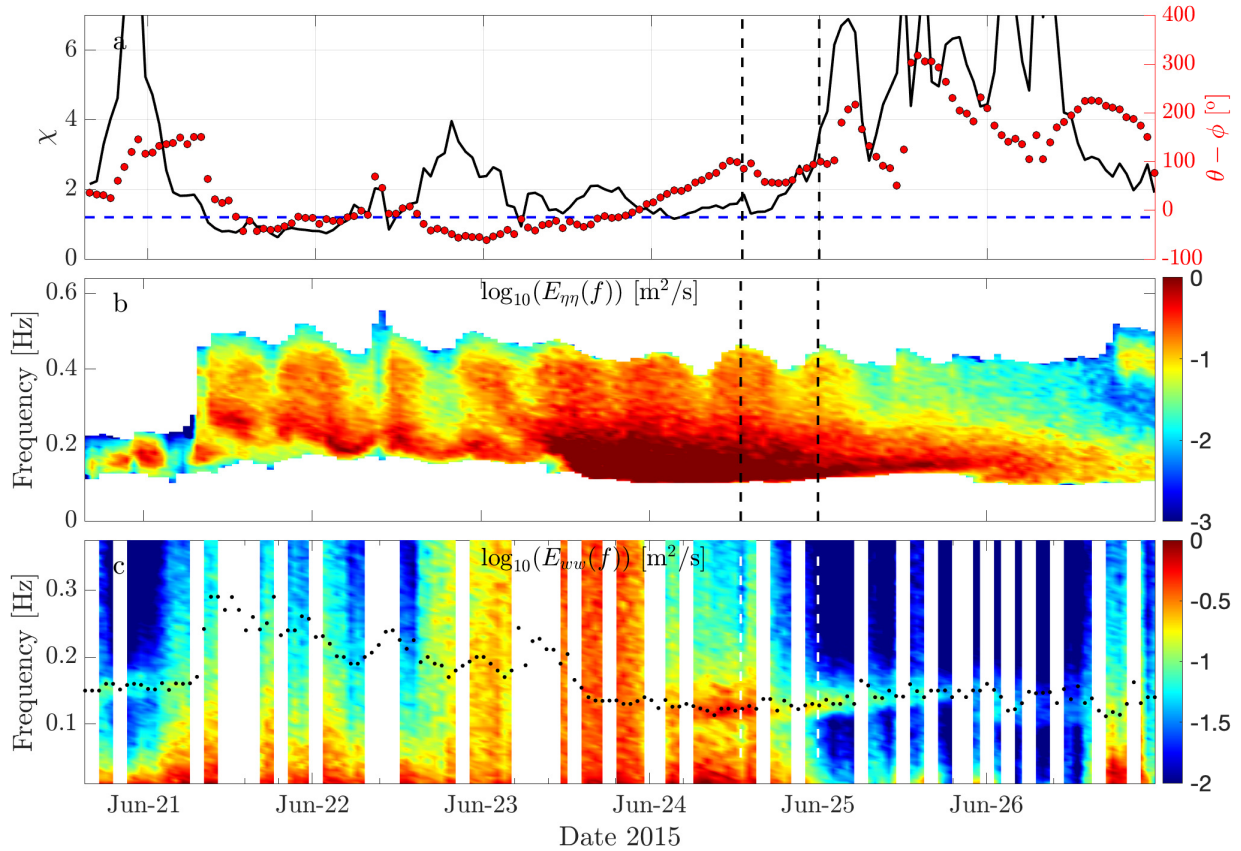
Figure 3. Time series of wave age $\chi = c_p/U_{10}$ in which U_{10} denotes the wind speed at 10 m and c_p is the phase speed. This figure contains the wind-wave misalignment timeseries $\theta - \theta_{wnd}$ where θ and θ_{wnd} denote the wave and wind directions respectively. The blue-dashed line ($\chi = 1.2$) represents the separation limit between the wind see and swell (i.e. $\chi \geq 1.2$); (b) spectral energy evolution of surface wave elevation η measured from AXYS buoy operating in very close vicinity of FINO1 met-mast; and (c) time evolution of energy spectra for the wind w-component in June 2015 between 21 and 27 calculated from the 15 m height sonic anemometer with a sampling frequency of 25 Hz. The black dotted markers are the wave peak frequency calculated from the buoy measured peak period T_p. Vertical grey dashed lines indicate the study cases.
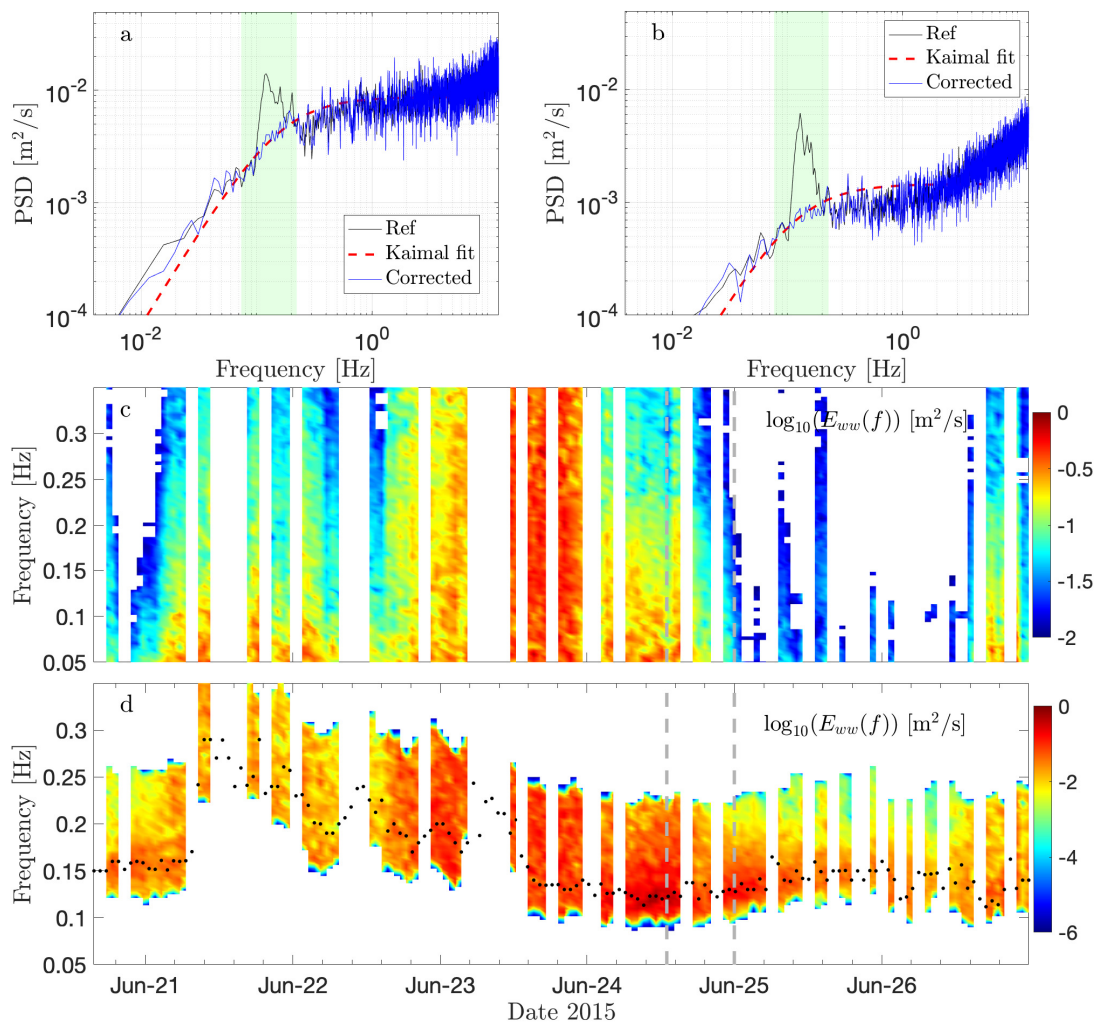
Figure 4. (a,b) Scaled power spectra of vertical velocity fluctuations w' for two events drawn as vertical grey dashed lines in Fig. 1a, and the corresponding corrected (decomposed) spectra (blue curves)). The red dashed lines show the spectral curves calculated from Eq. (2); and (c,d) energy-time spectra of decomposed vertical velocity w' and the wave-induced vertical velocity $\tilde{w}$ fluctuations by the use of suggested decomposition algorithm. The black dotted markers in (d) are the wave peak frequency from buoy measurements.
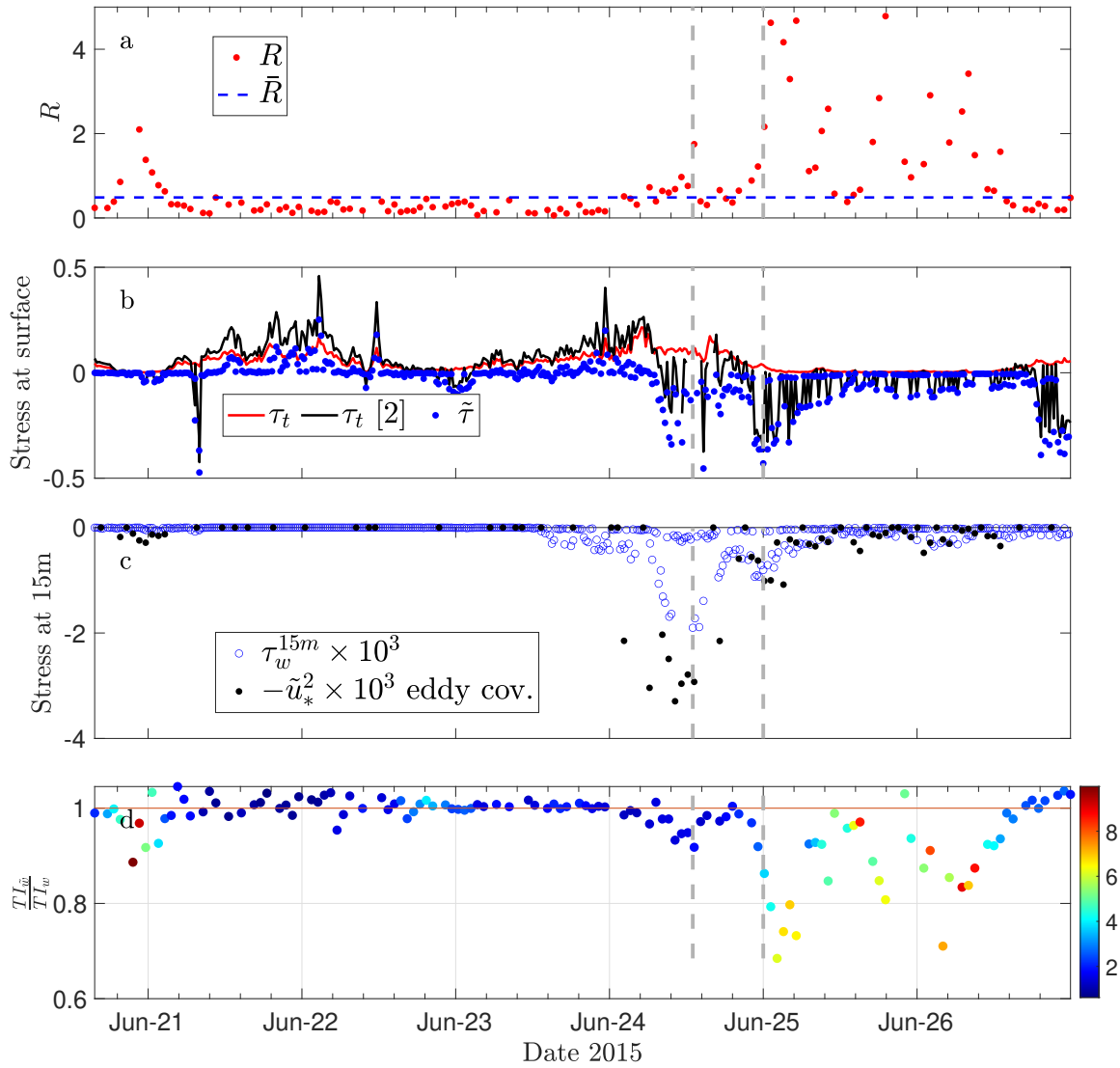
Figure 5. Time series of (a) the wave-turbulence strength ratio R; (b) momentum stresses at the surface calculated using COARE 3.6 algorithm (red line), Donelan et al. (1999) parameterization Eq. (11)), black line, and wave-induced momentum flux estimated from Eq. (12); and (c) the momentum fluxes at 15 m height estimated using decomposed turbulent wind data based on eddy covariance technique and the estimated wave-induced stress at the same height using Eq. (12) for $z = 15$ m.

and waves regimes. Under the wind-sea conditions, it was found that the wind stresses were almost similar to those observed under atmospheric neutral conditions. This is because the height of wave boundary layer was below the height of measurement,

170 and waves could contribute to a very small fraction of the total wind stress.

Code availability. Some codes for processing and plotting figures in this paper will be available on a valid access request.

Data availability. Time series of wind, wave age, and stability, covering yeardays between 160 and 210 2015, have been made available on https://doi.org/10.5281/zenodo.7422388. The OBLEX-F1 high frequency data (used in this study) at 15-m measured by sonic anemometer are on https://doi.org/10.5281/zenodo.7591198 and can be available through a valid access request.

175 *Author contributions.* The author proposed, implemented the methods and all signal processing, and wrote the manuscript.

Competing interests. The author declares that he has no competing of interest.

References

Bakhoday-Paskyabi, M., Fer, I., and Reuder, J.: Current and turbulence measurements at the FINO1 offshore wind energy site: analysis using 5-beam ADCPs, Ocean Dynamics, 68, 109–130, 2018.

Bakhoday-Paskyabi, M., Bui, H., and Mohammadpour Penchah, M.: Atmospheric-Wave Multi-Scale Flow Modelling, Delivery report, HIPERWIND EU project, No. 101006689, pp. 1–145, https://www.hiperwind.eu/publications, 2022.

Bricker, J. D. and Monismith, S. G.: Spectral Wave–Turbulence Decomposition, Journal of Atmospheric and Oceanic Technology, 24, 1479 – 1487, https://doi.org/10.1175/JTECH2066.1, 2007.

Carter, D.: Prediction of wave height and period for a constant wind velocity using the JONSWAP results, Ocean Engineering, 9, 17–33, https://doi.org/https://doi.org/10.1016/0029-8018(82)90042-7, 1982.

Chalikov, D.: The Parameterization of the Wave Boundary Layer, Journal of Physical Oceanography, 25, 1333 – 1349, https://doi.org/10.1175/1520-0485(1995)025<1333:TPOTWB>2.0.CO;2, 1995.

Chalikov, D. and Rainchik, S.: Coupled Numerical Modelling of Wind and Waves and the Theory of the Wave Boundary Layer, Boundary-Layer Meteorology, 138, 1–41, https://doi.org/10.1007/s10546-010-9543-7, 2011.

Davenport, A. G.: The spectrum of horizontal gustiness near the ground in high winds, Quarterly Journal of the Royal Meteorological Society, 87, 194–211, https://doi.org/https://doi.org/10.1002/qj.49708737208, 1961.

Donelan, M. A., Curcic, M., Chen, S. S., and Magnusson, A. K.: Wind-induced growth and attenuation of laboratory waves. Wind-over-Wave Couplings., Perspective and Prospects, S. G. Sajadi, N. H. Thomas, and J. C. R. Hunt, Eds., Clarendon Press, p. 183–194, 1999.

Donelan, M. A., Curcic, M., Chen, S. S., and Magnusson, A. K.: Modeling waves and wind stress, Journal of Geophysical Research: Oceans, 117, https://doi.org/https://doi.org/10.1029/2011JC007787, 2012.

Edson, J. B., Jampana, V., Weller, R. A., Bigorre, S. P., Plueddemann, A. J., Fairall, C. W., Miller, S. D., Mahrt, L., Vickers, D., and Hersbach, H.: On the Exchange of Momentum over the Open Ocean, Journal of Physical Oceanography, 43, 1589 – 1610, https://doi.org/10.1175/JPO-D-12-0173.1, 2013.

Gerbi, G. P., Trowbridge, J. H., Terray, E. A., Plueddemann, A. J., and Kukulka, T.: Observations of Turbulence in the Ocean Surface Boundary Layer: Energetics and Transport, Journal of Physical Oceanography, 39, 1077 – 1096, https://doi.org/10.1175/2008JPO4044.1, 2009.

Rieder, K. F., Smith, J. A., and Weller, R. A.: Observed directional characteristics of the wind, wind stress, and surface waves on the open ocean, Journal of Geophysical Research: Oceans, 99, 22 589–22 596, https://doi.org/https://doi.org/10.1029/94JC02215, 1994.

Semedo, A., Øyvind Saetra, Rutgersson, A., Kahma, K. K., and Pettersson, H.: Wave-Induced Wind in the Marine Boundary Layer, Journal of the Atmospheric Sciences, 66, 2256 – 2271, https://doi.org/10.1175/2009JAS3018.1, 2009.